Discrete Element Modelling of Rock Cutting

Jerzy Rojek, Eugenio Oñate, Carlos Labra and Hubert Kargl

Abstract This paper presents numerical modelling of rock cutting processes. The model consists of a tool-rock system. 3D geometry is considered in the model. The rock is modelled using the discrete element method, which is suitable to study problems of multiple material fracturing like that of rock cutting. The paper presents brief overview of the theoretical formulation and calibration of the discrete element model by simulation of the unconfined compressive strength (UCS) and indirect tension (Brazilian) tests. Numerical examples illustrate the paper. Rock cutting processes typical for underground excavation using both roadheader and TBM cutting tools are simulated. Numerical results are compared with the available experimental data.

1 Introduction

A variety of rock-cutting technologies is used in civil as well as in mining engineering. Figures 1a and 2a show machines performing rock cutting in underground excavation, a roadheader and a tunnel boring machine (TBM), respectively. Roadheaders excavate the rock by means of conical point attack picks (Figure 1b) mounted on a rotating cutterhead supported by a boom which is independently movable in the vertical and horizontal direction. In the excavation with TBMs, the rock is

Jerzy Rojek
Institute of Fundamental Technological Research, Polish Academy of Sciences, Pawińskiego 5B, 02-106 Warsaw, Poland; e-mail: jrojek@ippt.gov.pl

Eugenio Oñate · Carlos Labra
International Center for Numerical Methods in Engineering (CIMNE), Universidad Politécnica de Cataluña, Campus Norte UPC, 08034 Barcelona, Spain; e-mail: {onate, clabra}@cimne.upc.edu

Hubert Kargl
Sandvik Mining and Construction GmbH, Zeltweg, Austria; e-mail: hubert.kargl@sandvik.com

E. Oñate and R. Owen (eds.), *Particle-Based Methods*, Computational Methods in Applied Sciences 25, DOI 10.1007/978-94-007-0735-1_10,

(a)

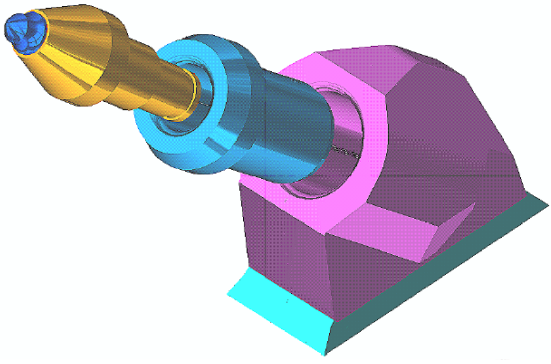

(b)

Fig. 1 Roadheader: (a) rock excavation with a roadheader, (b) typical design of a point attack pick

cut by means of cutter discs (Figure 2b) installed on a rotating cutter head, which is pressed against the tunnel face.

The basic physical phenomenon occurring during rock cutting is desintegration of the rock under mechanical action of a cutting tool. Design of cutting tools and setting parameters of cutting operations requires knowledge about the cutting process. Cutting force is one of the main factors characterizing a cutting process. Theoretical evaluation of the cutting force is not an easy task. Simple analytical models, like those developed by Evans [3] or by Nishimatsu [8], can provide an approximate estimation of cutting forces only.

Numerical simulation can provide valuable information about the cutting phenomenon. Numerical methods based on the continuum models, like finite element methods, have serious problems in modelling discontinuities of the material occurring during rock cutting [5]. The discrete element method takes into account all

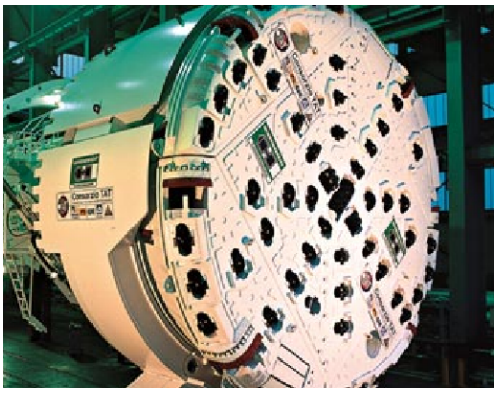

(a)

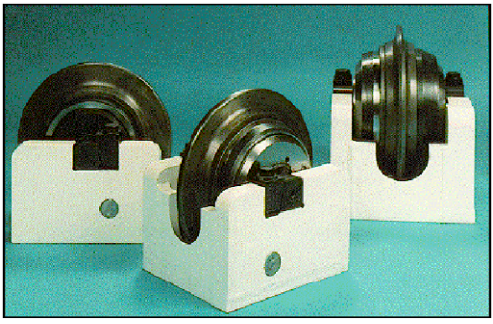

(b)

Fig. 2 TBM: (a) general view of a TBM cutterhead, (b) TBM disc cutters

kinds of discontinuities and material failure characterized with fracture and therefore is a suitable tool to study rock cutting [4, 11, 12].

2 Numerical Model of Rock Cutting

A system consisting of a tool and rock sample is considered in the model (Figure 3). The rock material is represented as a collection of spherical (in 3D) or cylindrical (in 2D) discrete elements interacting among themselves with contact forces. The tool is considered a rigid body with a surface discretised with triangular facets. The tool-rock interaction is modelled assuming Coulomb friction model. A numerical model of rock cutting has been developed within the authors' own implementation of the discrete element method (DEM) in the computer program DEMPack [9, 10].

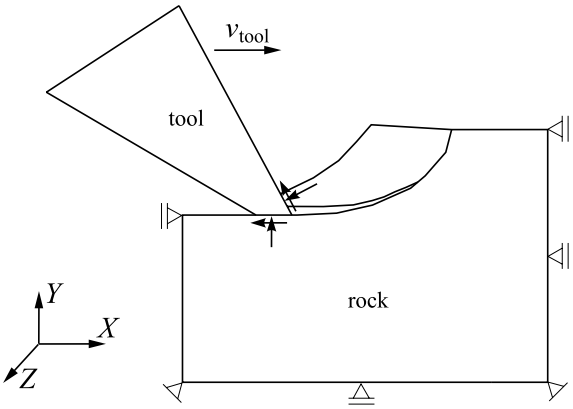

Fig. 3 Geometrical scheme of a rock cutting model

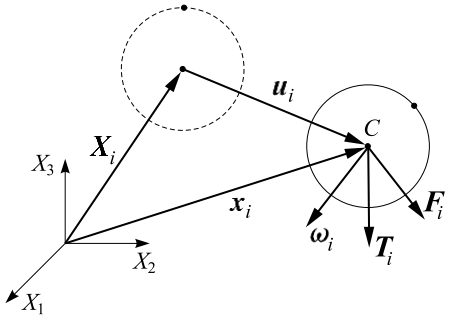

Fig. 4 Motion of a discrete element

3 Discrete Element Method Formulation

The translational and rotational motion of rigid spherical or cylindrical elements (particles) is governed by the standard equations of rigid body dynamics. For the i-th element (Figure 4) we have

$$m_i \ddot{\boldsymbol{u}}_i = \boldsymbol{F}_i \,, \tag{1}$$

$$J_i \dot{\boldsymbol{\omega}}_i = \boldsymbol{T}_i \,, \tag{2}$$

where $\boldsymbol{u}_i$ is the element centroid displacement in a fixed (inertial) coordinate frame $\boldsymbol{X}$, $\boldsymbol{\omega}_i$ – the angular velocity, m_i – the element mass, J_i – the moment of inertia, $\boldsymbol{F}_i$ – the resultant force, and $\boldsymbol{T}_i$ – the resultant moment about the central axes. The form of the rotational equation (2) is valid for spheres and cylinders (in 2D) and is simplified with respect to a general form for an arbitrary rigid body with the rotational inertial properties represented by a second order tensor. Vectors $\boldsymbol{F}_i$ and $\boldsymbol{T}_i$ are sums of:

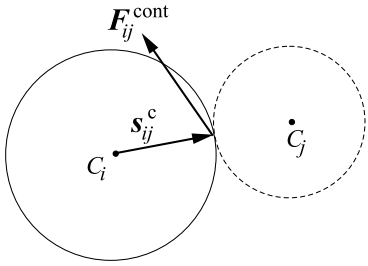

Fig. 5 Contact interaction between two discrete elements

- all forces and moments applied to the i-th element due to external load, $\boldsymbol{F}_i^{\text{ext}}$ and $\boldsymbol{T}_i^{\text{ext}}$, respectively,
- contact interactions with neighbouring spheres $\boldsymbol{F}_{ij}^{\text{cont}}$, $j = 1, \ldots, n_i^{\text{c}}$, where n_i^{c} are the number of elements being in contact with the i-th discrete element,
- forces and moments resulting from external damping, $\boldsymbol{F}_i^{\text{damp}}$ and $\boldsymbol{T}_i^{\text{damp}}$, respectively

$$\boldsymbol{F}_i = \boldsymbol{F}_i^{\text{ext}} + \sum_{j=1}^{n_i^{\text{c}}} \boldsymbol{F}_{ij}^{\text{cont}} + \boldsymbol{F}_i^{\text{damp}}\,, \tag{3}$$

$$\boldsymbol{T}_i = \boldsymbol{T}_i^{\text{ext}} + \sum_{j=1}^{n_i^{\text{c}}} \boldsymbol{s}_{ij}^{\text{c}} \times \boldsymbol{F}_{ij}^{\text{cont}} + \boldsymbol{T}_i^{\text{damp}}\,, \tag{4}$$

where $\boldsymbol{s}_{ij}^{\text{c}}$ is the vector connecting the centre of mass of the i-th element with the contact point with the j-th element (Figure 5).

Equations of motion (1) and (2) are integrated in time using the central difference scheme. The time integration operator for the translational motion at the n-th time step is as follows:

$$\ddot{\boldsymbol{u}}_i^n = \frac{\boldsymbol{F}_i^n}{m_i}\,, \tag{5}$$

$$\dot{\boldsymbol{u}}_i^{n+1/2} = \dot{\boldsymbol{u}}_i^{n-1/2} + \ddot{\boldsymbol{u}}_i^n \Delta t\,, \tag{6}$$

$$\boldsymbol{u}_i^{n+1} = \boldsymbol{u}_i^n + \dot{\boldsymbol{u}}_i^{n+1/2} \Delta t\,. \tag{7}$$

The first two steps in the integration scheme for the rotational motion are identical to those given by Eqs. (5) and (6):

$$\dot{\boldsymbol{\omega}}_i^n = \frac{\boldsymbol{T}_i^n}{J_i}\,, \tag{8}$$

$$\boldsymbol{\omega}_i^{n+1/2} = \boldsymbol{\omega}_i^{n-1/2} + \dot{\boldsymbol{\omega}}_i^n \Delta t\,. \tag{9}$$

The vector of incremental rotation $\Delta\boldsymbol{\theta}_i$ is calculated as

$$\Delta\boldsymbol{\theta}_i = \boldsymbol{\omega}_i^{n+1/2}\Delta t\,, \tag{10}$$

If necessary it is also possible to track the total change of rotational position of particles [1].

Explicit integration in time yields high computational efficiency of the solution for a single step. The disadvantage of the explicit integration scheme is its conditional numerical stability imposing the limitation on the time step Δt. The time step Δt must not be larger than a critical time step Δt_{cr}

$$\Delta t \le \Delta t_{\mathrm{cr}} \tag{11}$$

determined by the highest natural frequency of the system $\nu_{\max}$

$$\Delta t_{\mathrm{cr}} = \frac{2}{\nu_{\max}}\,. \tag{12}$$

Exact determination of the highest frequency $\nu_{\max}$ would require solution of the eigenvalue problem defined for the whole system of connected rigid particles. The maximum frequency of the whole system can be estimated as the maximum of natural frequencies ν_i^e of subsets of connected particles surrounding each particle e, cf. [2]:

$$\nu_{\max} \le \nu_{\max}^D\,, \quad \text{where} \quad \nu_{\max}^D = \max_{i,e}\nu_i^e \tag{13}$$

The contact force between two elements[1] $\boldsymbol{F}^{\mathrm{cont}}$ can be decomposed into normal and tangential components, $\boldsymbol{F}_{\mathrm{n}}^{\mathrm{cont}}$ and $\boldsymbol{F}_{\mathrm{t}}^{\mathrm{cont}}$, respectively

$$\boldsymbol{F}^{\mathrm{cont}} = \boldsymbol{F}_{\mathrm{n}}^{\mathrm{cont}} + \boldsymbol{F}_{\mathrm{t}}^{\mathrm{cont}} = F_{\mathrm{n}}^{\mathrm{cont}}\boldsymbol{n} + \boldsymbol{F}_{\mathrm{t}}^{\mathrm{cont}}\,, \tag{14}$$

where $\boldsymbol{n}$ is the unit vector normal to the particle surface at the contact point.

The contact forces $F_{\mathrm{n}}^{\mathrm{cont}}$ and $\boldsymbol{F}_{\mathrm{t}}^{\mathrm{cont}}$ are obtained using a constitutive model formulated for the contact between two rigid spheres. In the present work rock materials are modelled using elastic perfectly brittle model of contact interaction, where we assume initial bonding for the neighbouring particles. These bonds can be broken under load allowing us to simulate initiation and propagation of material fracture. Contact laws for the normal and tangential direction for the elastic perfectly brittle model are shown in Figure 6. When two particles are bonded the contact forces in both normal and tangential directions are calculated from the linear constitutive relationships:

$$F_{\mathrm{n}}^{\mathrm{cont}} = k_{\mathrm{n}}u_{\mathrm{n}}\,, \tag{15}$$

$$\|\boldsymbol{F}_{\mathrm{t}}^{\mathrm{cont}}\| = k_{\mathrm{t}}\,\|\boldsymbol{u}_{\mathrm{t}}\|\,, \tag{16}$$

where $F_{\mathrm{n}}^{\mathrm{cont}}$ – normal contact force, $\boldsymbol{F}_{\mathrm{t}}^{\mathrm{cont}}$ – tangential contact force, k_{n} – interface stiffness in the normal direction, k_{t} – interface stiffness in the tangential direction, u_{n} – normal relative displacement, $\boldsymbol{u}_{\mathrm{t}}$ – tangential relative displacement.

[1] In the next part of this section indices denoting the elements will be omitted.

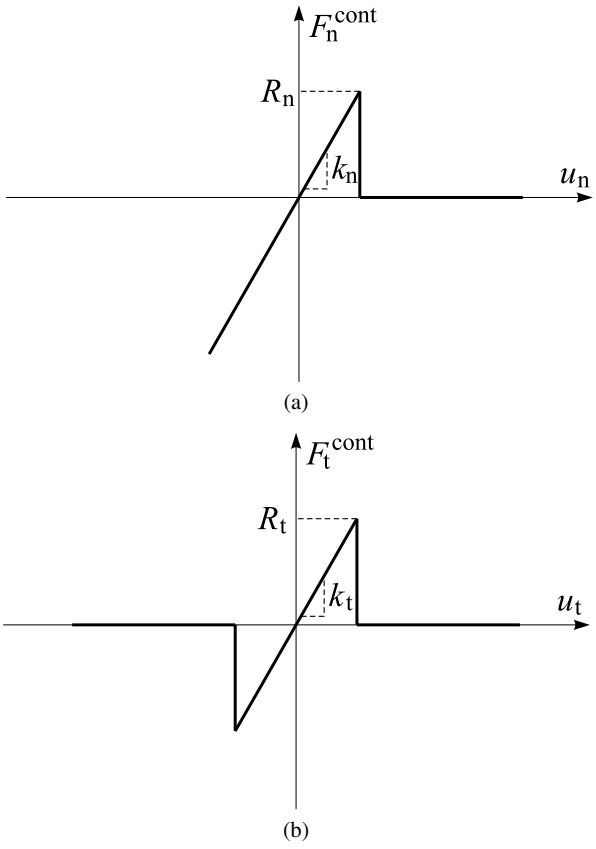

Fig. 6 Force-displacement relationships for the elastic perfectly brittle model: (a) in the normal direction, (b) in the tangential direction

Cohesive bonds are broken instantaneously when the interface strength is exceeded in the tangential direction by the tangential contact force or in the normal direction by the tensile contact force. The failure (decohesion) criterion can be written as

$$F_{\mathrm{n}}^{\mathrm{cont}} \leq R_{\mathrm{n}}\,, \tag{17}$$

$$\|\boldsymbol{F}_{\mathrm{t}}^{\mathrm{cont}}\| \leq R_{\mathrm{t}}\,, \tag{18}$$

where R_{n} – interface strength in the normal direction, R_{t} – interface strength in the tangential direction.

In the absence of cohesion the normal contact force can be compressive only ($R_n \leq 0$) and tangential contact force can be nonzero due to friction

$$\|\boldsymbol{F}_{\mathrm{t}}^{\mathrm{cont}}\| = \mu |F_{\mathrm{n}}^{\mathrm{cont}}| \tag{19}$$

if $R_{\mathrm{n}} < 0$ or zero otherwise. The friction force is given by Eq. (19) expressing the Coulomb friction law, with μ being the Coulomb friction coefficient.

A quasi-static state of equilibrium of the assembly of particles can be achieved by application of adequate damping. Damping is necessary to dissipate kinetic energy. Damping terms $\boldsymbol{F}_i^{\mathrm{damp}}$ and $\boldsymbol{T}_i^{\mathrm{damp}}$ in equations (3) and (4) in the present work are of non-viscous type and are given by

$$\boldsymbol{F}_i^{\mathrm{damp}} = -\alpha^t \|\boldsymbol{F}_i^{\mathrm{ext}} + \boldsymbol{F}_i^{\mathrm{cont}}\| \frac{\dot{\boldsymbol{u}}_i}{\|\dot{\boldsymbol{u}}_i\|}, \tag{20}$$

$$\boldsymbol{T}_i^{\mathrm{damp}} = -\alpha^r \|\mathbf{T}_i\| \frac{\omega_i}{\|\omega_i\|}, \tag{21}$$

where α^t and α^r, are respective damping constants for translational and rotational motion.

4 Determination of Rock Model Parameters

The discrete element model can be regarded as a micromechanical material model, the contact model parameters being micromechanical parameters. Assumption of adequate micromechanical parameters yield required macroscopic rock properties, the most important being the Young modulus E, Poisson's coefficient μ, compressive strength σ_{c} and tensile strength σ_{t}. For the elastic-brittle model of interaction between discrete elements described in Section 3 we have the following set of constitutive parameters:

k_{n} – contact stiffness in the normal direction,
k_{t} – contact stiffness in the tangential direction,
R_{n} – interface strength in the normal direction,
R_{t} – interface strength in the tangential direction,
μ – Coulomb friction coefficient,
α^t – damping coefficient for translational motion,
α^r – damping coefficient for rotational motion.

Determination of the model parameters is the key issue in the use of the discrete element method.

4.1 Dimensionless Micro-Macro Relationships

In the present work the micromechanical parameters have been determined using the methodology developed by Huang [4] based on the combination of the dimensional analysis with numerical simulation of the standard laboratory tests for rocks,

unconfined compression test and Brazilian test. Dimensional analysis is based on the Buckingham π theorem, which states that any physically meaningful functional relationship of N variables $\Psi(Q_1, Q_2, \ldots, Q_N)$ can be expressed equivalently by a function of $N - r$ dimensionless parameters $\Phi(\pi_1, \pi_2, \ldots, \pi_{N-r})$, where r is the number of primary dimensions (minimum independent dimensions required to specify the dimensions of all the relevant parameters), and $N - r$ is the maximum number of independent parameters [7].

Here we will search functions defining the macroscopic material parameters: Young's modulus E, Poisson's ratio ν, compressive strength σ_c and tensile strength σ_t in terms of microscopic parameters: k_n, k_t, R_n, R_t, μ, α^t, α^r. Macroscopic properties can also depend on other parameters, like particle size characterized by the average radius r, material density ρ, porosity of the particle assembly n. The set of the parameters can be completed with geometrical parameters represented by the specimen size L (due to possible scale effect) and loading velocity V. Thus, the number of relevant parameters N is 12. We have three primary dimensions involved: mass, length, time ($r = 3$). We can assume there are nine independent parameters.

The set of parameters is not unique and can be modified by taking into account some other parameters that can influence macroscopic properties. In [13] the minimum and maximum element radii, r_{min} and r_{max}, respectively, have been included to the relevant parameters, in order to better consider the influence of the element size distribution on macroscopic properties. To some extent, this influence is taken in our formulation by the porosity n which depends on the size distribution, the wider size distribution the lower porosity in the discrete element model can be achieved.

Having in mind there are alternative approaches, our procedure is based on the following set of nine independent parameters: $\{k_n r/R_n,\ R_t/R_n,\ k_t/k_n,\ n,\ r/L,\ \mu,\ \alpha^t,\ \alpha^r,\ V/\sqrt{k_n/\rho}\}$. Since the material properties will be studied under quasi-static conditions, the set of parameters can be reduced by removing $V/\sqrt{k_n/\rho}$, α^t and α^r. Further on, assuming that the element size r is small compared to macroscopic dimension L ($r \ll L$), we can neglect the influence of the parameter r/L. The friction coefficient μ has influence mainly on the post-failure material behaviour, so we can omit it in the relationships for elastic constants and strength parameters. The set of relevant dimensionless parameters is reduced to the following one: $\{k_n r/R_n,\ R_t/R_n,\ k_t/k_n,\ n\}$. Assuming that the elastic constants are determined in the range in which the failure is not initiated yet, in the relationships for elastic constants we can consider only two dimensionless parameters: $\{k_t/k_n,\ n\}$. Since constitutive relationships for 2D are given for the depth (the third dimension) of 1 m, the parameters for 2D have different meaning and dimensions from those for 3D. Therefore we have to consider separately the cases of 2D and 3D. The behaviour of the discrete element model in 2D and 3D is also different – this is another reason why the dimensionless relationships for 2D and 3D are different.

4.1.1 Dimensionless Micro-Macro Relationships for 2D Problems

Following [4] the following dimensionless functional relationships linking macroscopic and microscopic parameters have been postulated for the 2D discrete element model:

$$\frac{E}{k_n} = \Phi_E^{2D}\left(\frac{k_T}{k_n}, n\right), \tag{22}$$

$$\nu = \Phi_\nu^{2D}\left(\frac{k_T}{k_n}, n\right), \tag{23}$$

$$\frac{\sigma_c r}{R_n} = \Phi_c^{2D}\left(\frac{R_T}{R_n}, \frac{k_T}{k_n}, n\right), \tag{24}$$

$$\frac{\sigma_t r}{R_n} = \Phi_t^{2D}\left(\frac{R_T}{R_n}, \frac{k_T}{k_n}, n\right). \tag{25}$$

The specific form of the dimensionless relationships (22)–(25) have been obtained from the results of numerical simulations of the unconfined compression test (UCS) and Brazilian tests. The results of a simulation of the UCS test are presented in Figure 7 in the form of failure evolution with distribution of stresses in the direction of loading. The material sample of 50 × 50 mm represented by an assembly of randomly compacted 4979 discs of radii 0.262–0.653 mm (average radius 0.465 mm) has been generated using the high density sphere packing algorithm developed in [6]. Compaction of the particle assembly has been characterized by a porosity n of 13%. The stress-strain curve obtained in the analysis (Figure 8) can be used to determine the Young modulus E and compressive strength σ_c. The simulation provides the value of the Poisson ratio ν, as well.

The cylindrical specimen of the diameter 50 mm for the simulation of the Brazilian test has been obtained by trimming adequately the specimen used in the UCS modelling. The failure mode with distributions of averaged stresses in the direction normal to the loading is shown in Figure 9. The failure in the form of splitting along the diameter parallel to the loading predicted in simulation agrees very well with the experimental observations. The stress distribution is in a very good agreement with theoretical solutions [14].

The force-time curve obtained in the simulation is plotted in Figure 10. Taking the maximum force $P_{\max}$ we find the tensile strength as:

$$\sigma_t = \frac{2P_{\max}}{\pi L D} \tag{26}$$

Simulations of both the UCS and Brazilian test have been performed for the dimensionless parameter k_t/k_n in the range from 0 to 2, assuming $R_t/R_n = 1$. The curves representing the dimensionless relationships (22) and (23) are plotted in Figure 11, the curves corresponding to the relationships (24) and (25) are shown in Figure 12.

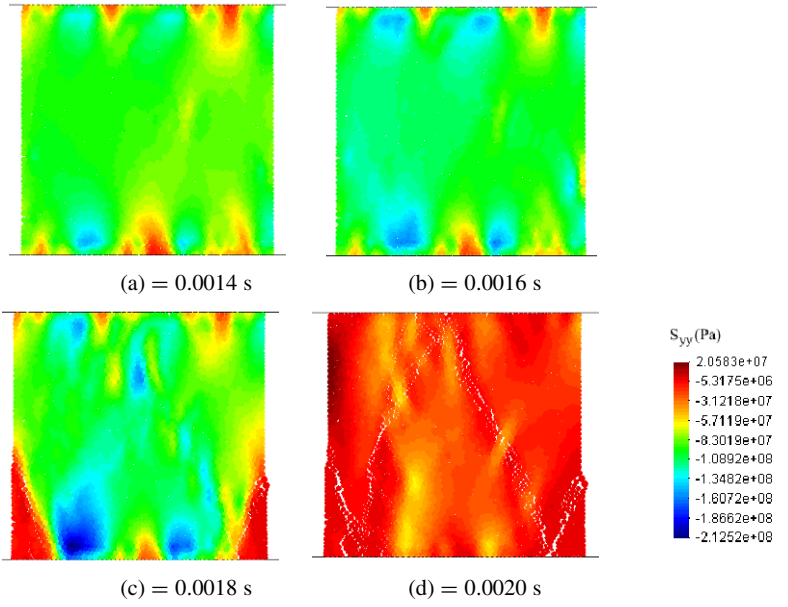

Fig. 7 Simulation of unconfined compression test – failure evolution with distribution of stress along the loading direction

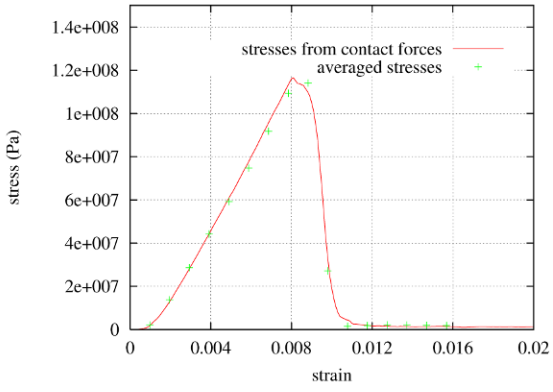

Fig. 8 Simulation of unconfined compression test – stress-strain curve

4.1.2 Dimensionless Micro-Macro Relationships for 3D Problems

The methodology developed for 2D models has been extended in this work on the three-dimensional discrete element modelling. Analogically to Eqs. (22)–(25) the following dimensionless functional relationships for 3D discrete element models have been postulated:

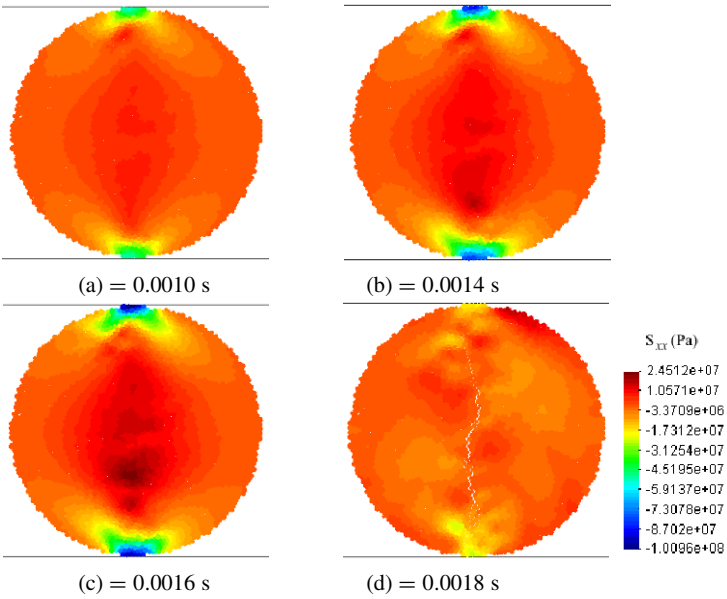

Fig. 9 Simulation of Brazilian test – failure of the rock sample with distribution of stress in the direction normal to the loading

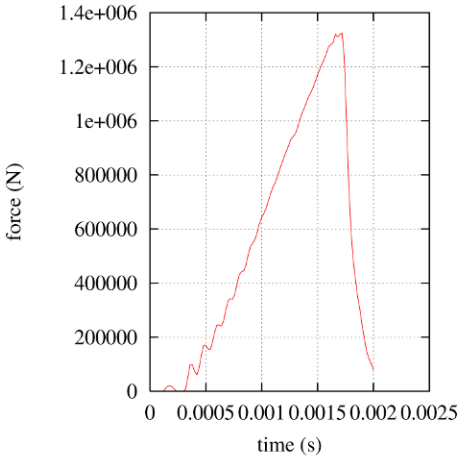

Fig. 10 Simulation of the Brazilian test – load-time curve

$$\frac{Er}{k_n} = \Phi_E^{3D}\left(\frac{k_T}{k_n}, n\right), \tag{27}$$

$$\nu = \Phi_\nu^{3D}\left(\frac{k_T}{k_n}, n\right), \tag{28}$$

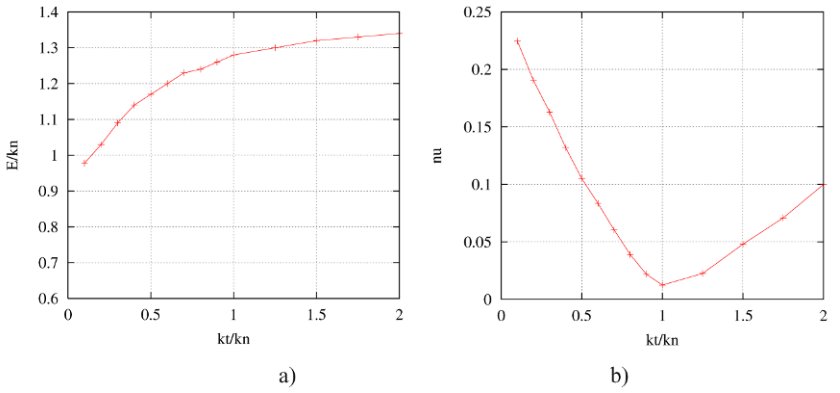

Fig. 11 Dimensionless relationships between the microscopic parameters and macroscopic elastic constants: (a) relationship for Young's modulus, (b) relationship for Poisson's ratio

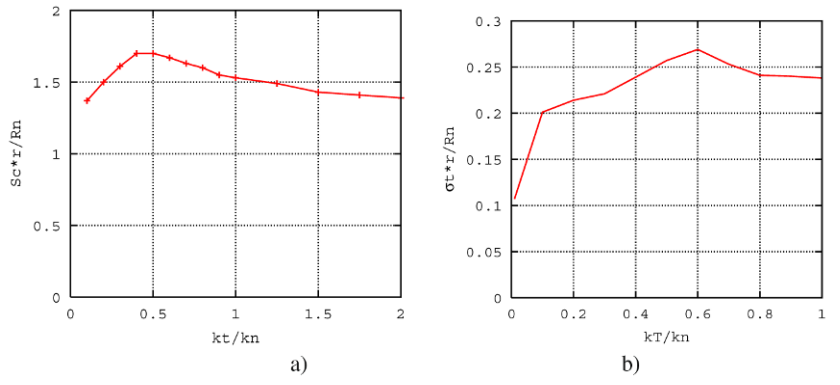

Fig. 12 Dimensionless relationships between the microscopic parameters and (a) compressive strength, (b) tensile strength.

$$\frac{\sigma_c r^2}{R_n} = \Phi_c^{3D}\left(\frac{R_T}{R_n}, \frac{k_T}{k_n}, n\right), \tag{29}$$

$$\frac{\sigma_t r^2}{R_n} = \Phi_t^{3D}\left(\frac{R_T}{R_n}, \frac{k_T}{k_n}, n\right). \tag{30}$$

The specific form of the dimensionless relationships have been obtained from the results of numerical simulations of the laboratory tests. Results of the numerical simulation of the UCS and Brazilian tests are shown in Figure 13. The failure obtained in simulation is similar to the failure observed in the experiments. The simulations have been performed for the dimensionless parameter k_t/k_n in the range from 0 to 1, assuming $R_t/R_n = 1$. The relationships (27), (28) and (29) obtained from the simulations of the UCS test are plotted in Figures 14 and 15a. The rela-

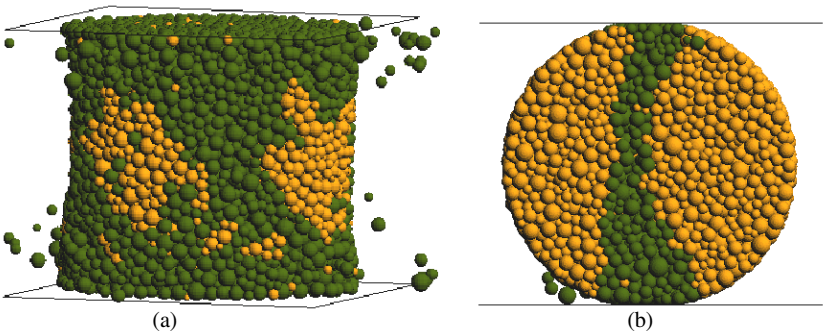

Fig. 13 Results of the numerical simulation of the laboratory tests for rocks: (a) unconfined compression test, (b) Brazilian test

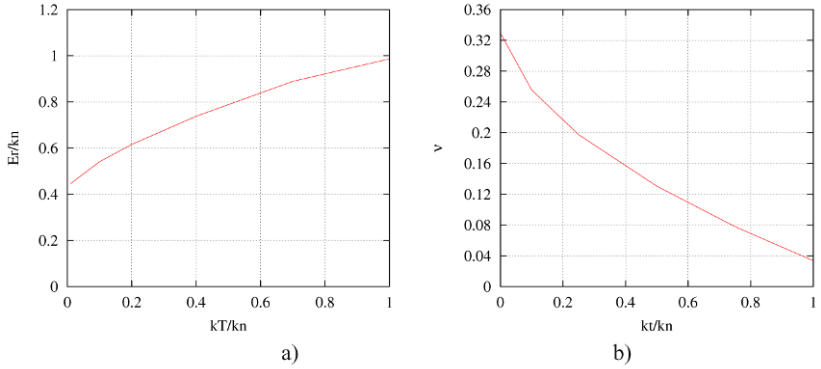

Fig. 14 Elastic dimensionless parameters as functions of k_t/k_n

tionship (30) obtained from the numerical simulations of the Brazilian test is given in Figure 15b.

5 Simulation of Rock Cutting

The discrete element model presented above has been applied to simulation of rock cutting. Two laboratory tests of rock cutting have been analysed, the first one consists of rock cutting with a single roadheader pick and the other one is the linear cutting test with a TBM disc cutter.

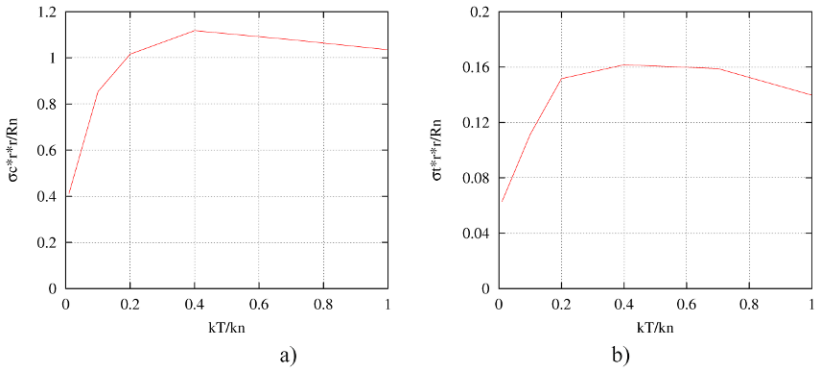

Fig. 15 Dimensionless compressive strength parameters as a function of k_t/k_n: (a) for compression, (b) for tension

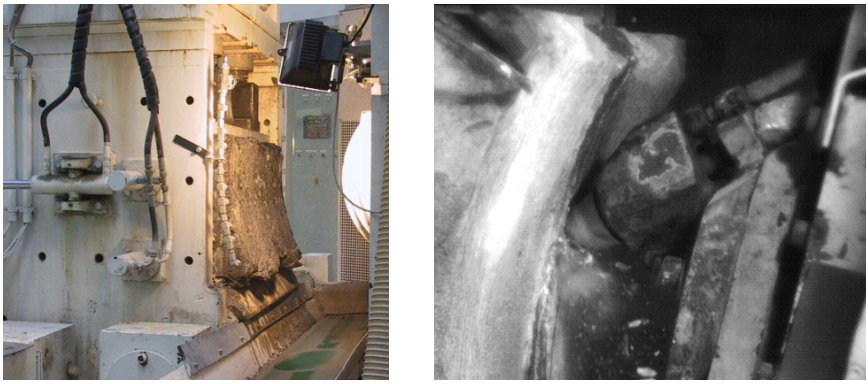

Fig. 16 Laboratory rock cutting test: (a) the cutting test rig, (b) rock cutting process (laboratory of Sandvik Mining and Construction GmbH, Zeltweg, Austria)

5.1 Simulation of Rock Cutting with a Single Roadheader Pick

Scale-one cutting tests with a single roadheader pick are performed on the cutting testrig (Figure 16) built in the laboratory of SANDVIK Mining and Construction (Zeltweg, Austria) to study cuttability of specific rocks and performance of cutting tools.

Cutting of a sandstone block by a rotating roadheader pick was chosen for numerical analysis. Mechanical properties of the rock have been determined experimentally and are the following: Young modulus $E = 18690$ MPa, compressive strength $\sigma_c = 127$ MPa and tensile strength $\sigma_t = 12$ MPa.

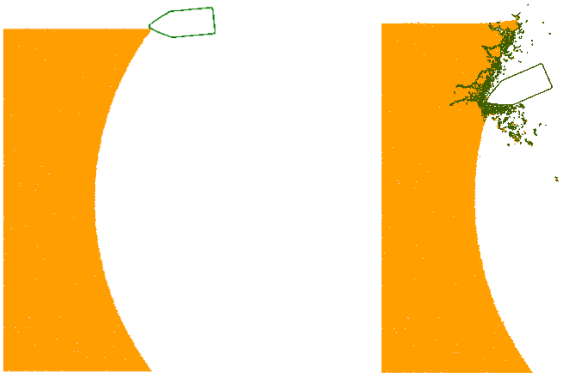

(a) (b)

Fig. 17 2D numerical simulation of rock cutting: (a) numerical model, (b) failure mode during rock cutting

5.1.1 2D Simulation of the Rock Cutting Test

A numerical model developed for simulation of the rock cutting test is shown in Figure 17a. The rock specimen is discretized using 30,750 cylindrical elements of radii $r = 1$–1.5 mm. Using the dimensionless relationships (22)–(24) the following set of microscopic parameters has been determined for the rock under consideration: $k_n = 1.61129 \cdot 10^{10}$ Pa, contact stiffness in the tangential direction $k_t = 0.3222 \cdot 10^{10}$ Pa, Coulomb friction coefficient $\mu = 0.839$ and cohesive bond strengths in the normal and tangential direction, $R_n = R_t = 0.29 \cdot 10^5$ N/m. The model parameters were verified by simulations of the UCS and Brazilian tests using specimens of similar characteristics as those of the rock specimen. The values of 118 MPa and 16.8 MPa were obtained for the compressive and tensile strengths, respectively. These values were accepted as satisfactorily agreeing with the experimental results.

The model of rock cutting was supplemented with the parameters of the rock-tool interaction and global damping. For the rock-tool interaction the following set of parameters has been assumed: $k_{\mathrm{n}} = k_{\mathrm{s}} = 5 \cdot 10^{10}$ MPa, $\mu = 0.5$. Non-viscous damping has been assumed taking the damping factors $\alpha^{\mathrm{nvt}} = \alpha^{\mathrm{nvr}} = 0.2$.

Figure 17b shows the rock failure mode obtained in the simulation. A satisfying accordance with the failure observed in the labratory test can be watched. Figure 18 shows variation of the cutting force obtained in the numerical simulation. The numerical cutting force is compared with the average experimental value. As it can be seen in Figure 18 the mean cutting force from the numerical analysis agrees quite well with the average experimental force (about 7000 kN).

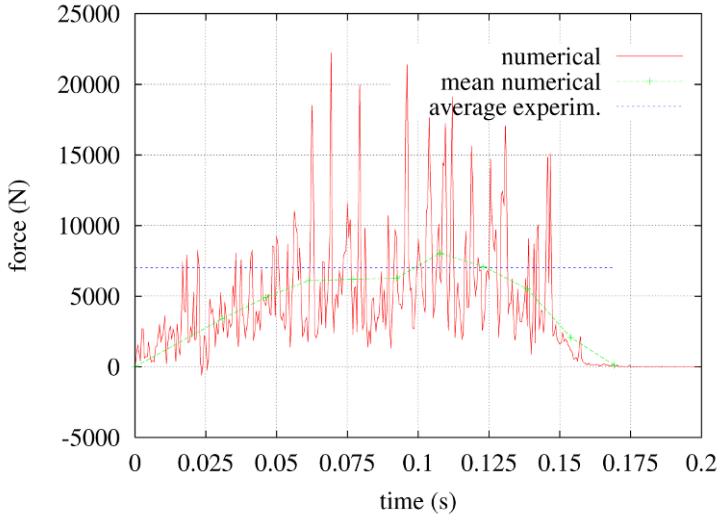

Fig. 18 2D numerical simulation of rock cutting – cutting force variation

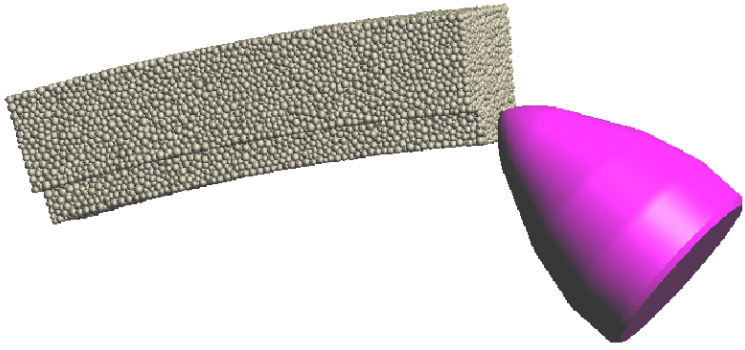

Fig. 19 3D numerical model of rock cutting

5.1.2 3D Simulation of the Rock Cutting Test

All the three components of a cutting force can be calculated using a three-dimensional model of the rock cutting test. The geometrical model created is shown in Figure 19. The material sample has been discretized using 71,200 spherical particles with average radius of 1.02 mm. The discrete element assembly has been generated using the high density sphere packing algorithm [6]. The tool was assumed rigid and its surface was discretized with a fine mesh of triangular facets representing accurately a complex tool tip geometry.

The micromechanical parameters for the rock considered were found with help of dimensionless relationships given in Figures 14a and 15a. First, the ratio between

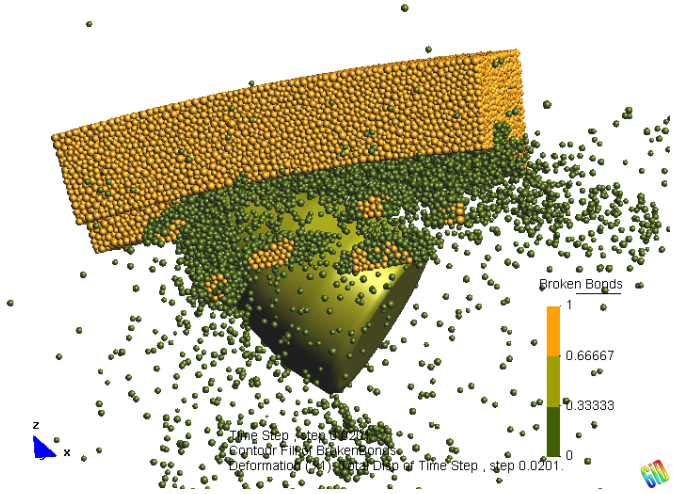

Fig. 20 Numerical simulation of the laboratory rock cutting test

the contact stiffness in the tangential and normal direction has been assumed 0.4, since for this value the brittle failure of rock in 3D simulations of the UCS and Brazilian test has been correctly reproduced. From the curve given in Figures 14a the contact stiffness in the normal direction $k_n = 2.6 \cdot 10^7$ N/m has been obtained, then we have the contact stiffness in the tangential direction $k_T = 1.04 \cdot 10^7$. The value of cohesive bond strengths in the normal R_n can be calculated from the plots in Figures 15a or 15b. The results obtained from these two plots are slightly different, $R_n = 117$ N from the plot in Figure 15a vs. $R_n = 90$ N from Figure 15b. Since the failure in cutting of sandstone is of brittle character and splitting of chips is mainly due to tensile stresses, the value $R_n = 90$ N according to the indirect tensile test simulation results has been adopted. Similar value for the shear bond strength has been taken, $R_T = 86$ N.

The results of numerical simulation are shown in Figure 20. Splitting of chips typical for brittle rock cutting can be seen. The three components of cutting forces obtained in simulation are plotted in Figure 21. Numerical forces are compared with experimental average measurements. Quite a good agreement can be observed.

5.2 Simulation of the Linear Cutting Test

The linear cutting test has been simulated. Figure 22 shows the model geometry, consisting of the disc cutter and a rock sample. Only the area of the cutter ring interacting directly with the rock is considered. A rock sample with dimensions of $400 \times 150 \times 50$ mm is represented by an assembly of randomly generated and densely compacted 40449 spherical elements of radii ranging from 0.8 to 6.0 mm. The granite properties are assumed in the simulation, appropriate DEM parameters being evaluated. The disc cutter is treated as a rigid body and discretized with

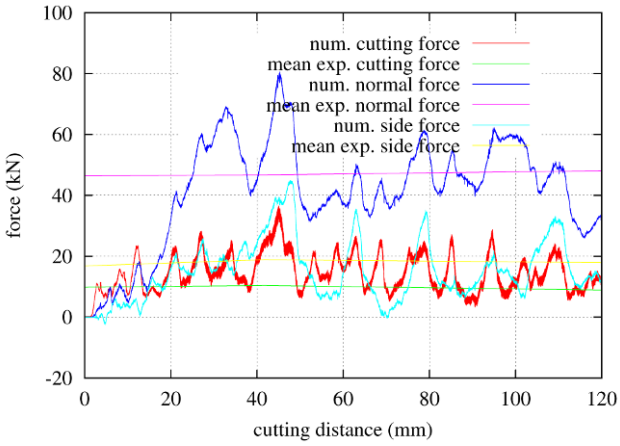

Fig. 21 Rock cutting forces – comparison of numerical results with experimental average values

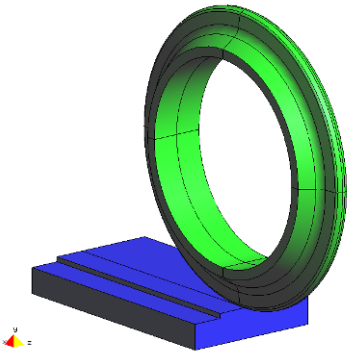

Fig. 22 Model geometry of the linear cutting test – model geometry

triangular facets. The parameters describing the disc interaction with the rock are as follows: contact stiffness modulus $k_n = 10$ GPa, Coulomb friction coefficient $\mu = 0.8$. The velocity of the disc cutter is assumed to be 10 m/s.

Figure 23 shows the cutter disc during cutting. Normal contact force history is shown in Figure 24. Numerical results have been compared with experimental ones provided by Herrenknecht AG. A good agreement between the numerical and average experimental values is clearly seen.

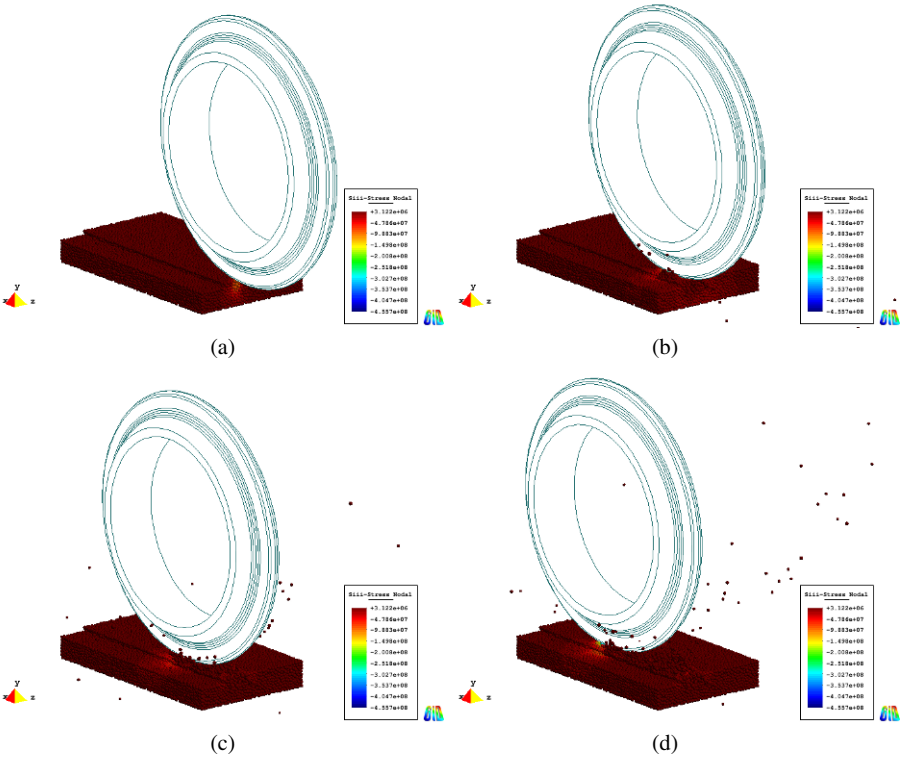

Fig. 23 Simulation of the linear cutting test – rock failure with distribution of macroscopic stresses (lowest principal stress – maximum compressive stress)

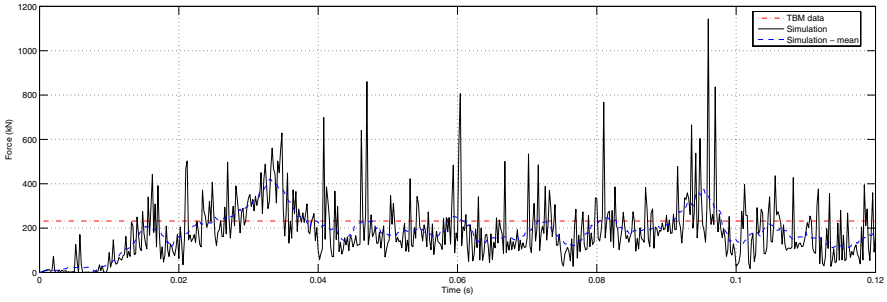

Fig. 24 Normal force history

6 Concluding Remarks

The three-dimensional discrete element model of rock cutting is capable to represent correctly complexity of a rock cutting process. A good qualitative and quantitative

agreement of numerical results with experimental measurements has been found out in the validation of the model developed in the present work. The discrete element model developed can be employed in the design of rock cutting tools and processes.

Acknowledgement

The authors acknowledge partial funding by the EU project TUNCONSTRUCT (contract no. IP 011817-2).

References

1. Argyris, J., An excursion into large rotations. *Comput. Meth. Appl. Mech. Eng.*, 32:85–155, 1982.
2. Belytschko, T., Smolinski, P., Liu, W.K., Stability of multi-time step partitioned integrators for the first order finite element systems. *Comput. Meth. Appl. Mech. Eng.*, 49:281–297, 1985.
3. Evans, I., The force required for pointed attack picks. *Int. J. Min. Engng.*, 2:63–71, 1965.
4. Huang, H., Discrete element modeling of tool-rock interaction. PhD Thesis, University of Minnesota, 1999.
5. Jonak, J., Podgórski, J., Mathematical model and results of rock cutting modelling. *Journal of Mining Science*, 37:615–618, 2001.
6. Labra, C., Oñate, E., High density sphere packing for discrete element method simulations. *Communications in Numerical Methods in Engineering*, 25(7):837–849, 2009.
7. Langhaar, H.L., *Dimensional Analysis and Theory of Models*. Wiley, 1951.
8. Nishimatsu, Y., The mechanics of rock cutting. *Int. J. Rock Mech. Mining Sci.*, 9:261–270, 1972.
9. Oñate, E., J. Rojek, J., Combination of discrete element and finite element methods for dynamic analysis of geomechanics problems. *Comput. Meth. Appl. Mech. Eng.*, 193:3087–3128, 2004.
10. Rojek, J., Oñate, E., Zarate, F., Miquel, J., Modelling of rock, soil and granular materials using spherical elements. In *2nd European Conference on Computational Mechanics ECCM-2001*, Cracow, 26–29 June, 2001.
11. Stavropoulou, M., Modeling of small-diameter rotary drilling tests on marbles. *Int. J. Rock Mech. Min. Sci.*, 43:1034–1051, 2006.
12. Su, O., Akcin, N.A., te Kamp, L., Modeling of cutting forces acting on a conical pick. In *Proc. of EURO:TUN 2009 II International Conference on Computational Methods in Tunnelling*, Bochum, Germany, 2009.
13. Yang, B., Jiao, Y., Lei, S., A study on the effects of microparameters on macroproperties for specimens created by bonded particles. *Eng. Comput.*, 23(6):607–631, 2006.
14. Yua, Y., Yinb, J., Zhong, Z., Shape effects in the Brazilian tensile strength test and a 3D FEM correction. *Int. J. Rock Mech. Min. Sci.*, 43:623–627, 2006.